

Tuning the Electrochemical Performance of Multiple Phased Selenides@C/MXene Composites via Controllable Synthesis of Multivariate Metal-Organic Frameworks

Weiquan Liang,^[a] Mingjie Liu,^[a] Xiaoyan Shi,*^[a] Bin Chen,^[a] Lianyi Shao,^[a] Junling Xu,^[a] and Zhipeng Sun*^[a]

Metal-organic frameworks (MOFs) are excellent precursors for electrode materials preparations. Synergistic effects may exist between different metal centers in multivariate MOFs, making them often more effective than single-metal MOFs. Herein, we propose an atom economic mechanochemical method to realize the efficient component regulation of target multivariate MOFs. Moreover, by combining the synthesis of multivariate MOFs and exfoliating MXene, multivariate MOF/MXene composites can be obtained via a one-step strategy. A further selenization process can derive them into selenides@C/MXene composites. These derived composites contain multiple nanostructured metal selenides embedded in multi-heteroatom doped carbon matrix. For these composites, abundant heterojunction structures are formed, which can build internal self-

built electric field and enhance the reaction kinetics effectively for sodium-ion storage. More importantly, the electrochemical performance of NCMS@C/MX composites can be optimized due to the intrinsic characteristics of the containing metal selenides. Overall, experimental results demonstrate the universality of this solvent-free synthesis route for controllable preparation of high-performance selenides@C/MXene electrode materials. It provides a feasible and environmentally friendly method to adjust metal ratios for optimal energy storage performance. We hope this research inspires optimization strategies for high-performance electrode materials and leads to the development of energy storage materials with more rational structures and better performance.

Introduction

Metal-organic frameworks (MOFs) derivatives are attracting attention in the field of electrochemical energy storage due to their characteristics, such as large specific surface area and easily controllable constitutions.^[1–6] In particular, synergistic effects may exist between different metal centers in multivariate MOFs, making them often more effective than single-metal MOFs.^[7–9] Also, by precisely controlling the metal ratio of multivariate MOFs, it is possible to prepare better ternary system electrode materials in a cost-effective manner.^[10–14] This is also true when it comes to the multivariate MOFs-derived electrode materials. Multivariate MOFs are typically synthesized through a simple one-step process, streamlining the procedure and increasing efficiency.^[15,16] In addition, the pursuit of low-carbon motivates the development of synthesis routes with more environmentally friendly and green features.^[17,18]

Mechanochemical ball-milling is an efficient strategy for synthesizing MOFs due to its greenness and atom economy characteristics.^[19–22] Compared to common preparation meth-

ods, such as solvothermal synthesis, ball-milling can often prepare MOFs in a shorter time and under milder conditions. It produces almost no chemical waste and does not require any solvents throughout the process.^[19,20,23–25] Previously, the application of mechanically synthesized pristine MOFs in energy storage areas was limited by their poor crystallinity.^[26] However, this is not necessarily true when focusing on MOF-derived electrode materials. In our previously reported work, the electrochemical performance of derivatives from mechanochemically synthesized single-metal MOF is comparable to that of previously reported MOF derivatives prepared by traditional solvent methods.^[26]

Moreover, for traditional solvent-based methodology, the ratio between metal centers in multivariate MOFs can be tuned via controlling the proportion of reactants only when the chemically resembled transition metals are used, such as nickel and cobalt.^[27] It often goes beyond control when it comes to the metal centers with different coordination behaviors. The mechanical strategy could be the solution to the issues mentioned above due to its atom economy character. Therefore, introducing mechanochemical ball-milling into the synthesis of multivariate MOFs has a solid foundation.

Besides, MXenes with layered structures are well known for their high specific surface area, superior conductivity, and good mechanical strength.^[28–32] Therefore, they are often introduced to construct high-performance composite electrode materials, acting as electron conducting agents, morphology inducing agents, as well as structure support.^[33]

[a] W. Liang, M. Liu, Dr. X. Shi, B. Chen, Dr. L. Shao, Dr. J. Xu, Prof. Z. Sun
School of Materials and Energy
Guangdong University of Technology
Guangzhou, 510006, Guangdong (P.R. China)
E-mail: shixy222@gdut.edu.cn
zpsunxj@gdut.edu.cn

 Supporting information for this article is available on the WWW under
<https://doi.org/10.1002/batt.202300462>

Previous reports show that composites based on layered/few-layered MXenes often result in a more efficient phase contact or interface, achieving better performance.^[34,35] However, the delamination process of MXenes can be complex and cumbersome. For instance, specific dispersants should be carefully chosen, and low delamination efficiency and large raw material loss are common issues when preparing layered/few-layered MXenes. All above issues would definitely hinder its further application.^[36–38] In our previous reported work, we managed to prepare MOF/MXene composites in a one-step solvent-free process and derive them into electrode materials with excellent performance. The composite electrode materials with a few-layered MXene support system showed promoted electron transfer properties, improved electrochemical reaction kinetics, and alleviated volume expansion.^[26]

With all above in mind, the environmentally benign mechanochemical ball-milling method is introduced into the design and preparation of multivariate MOF/MXene composites.^[39,40] This strategy can effectively avoid the following issues during the synthesis procedure: *i*) the low efficiency while preparing the few-layer MXenes, *ii*) the harsh preservation condition of few-layer MXene solutions, *iii*) as well as the difficulties in the control of metal centers ratio in multivariate MOFs.^[41–43] In this work, a series of multivariate MOF/MXene composites with different metal ratios were synthesized and derived into corresponding selenides@C/MXene composites. Based on our previous work, the cyclophosphazene-based ligand is continued to be applied while constructing multivariate MOF/MXene composites. Three transition metal elements Ni, Co, and Mo were chosen as the metal centers due to the specialties of their selenides in the sodium storage area (Ni for high reactivity, Co and Mo for good reversibility). After that, the

performances of as-prepared selenides@C/MXene composites as sodium-ion battery anodes are evaluated. The results proved that their electrochemical performance can be tuned by the controllable constitutions. This work provides a new strategy for design and preparation of high-performance electrode materials for energy storage applications.

Results and Discussion

Synthesis and characterization

To investigate the effect of metal species and their ratios on the electrochemical properties, multivariate MOF/MXene composites with different metal center ratios of Ni, Co, and Mo were prepared and derived into corresponding selenides@C/MXene, denoted as NCMS@C/MX. Figure 1(a) shows the synthesis illustration of NCMS@C/MX composites. With ball milling of the metal salts, ligands, and MXene together, and a followed-up selenization process, six types of NCMS@C/MX composites were prepared. They are NCMS@C/MX-011(Co:Mo=1:1), NCMS@C/MX-101(Ni:Mo=1:1), NCMS@C/MX-111 (Ni:Co:Mo=1:1:1), NCMS@C/MX-112 (Ni:Co:Mo=1:1:2), NCMS@C/MX-121 (Ni:Co:Mo=1:2:1), and NCMS@C/MX-211 (Ni:Co:Mo=2:1:1), respectively. More details about the preparation can be found in the supporting information.

Powder X-ray diffraction (XRD) characterization was used to obtain physical information about the composite materials (Figure 1b). The XRD spectrum of NCMS@C/MX-121 well corresponds to Ni_3Se_4 (JCPDS: 18-0890), CoSe_2 (JCPDS: 09-0234), and Mo_3Se_4 (JCPDS: 21-0575) phases. The peak corresponding to Mo_3Se_4 is not obvious. This may be due to the low crystallinity of this phase. Compared to NCMS@C/MX-

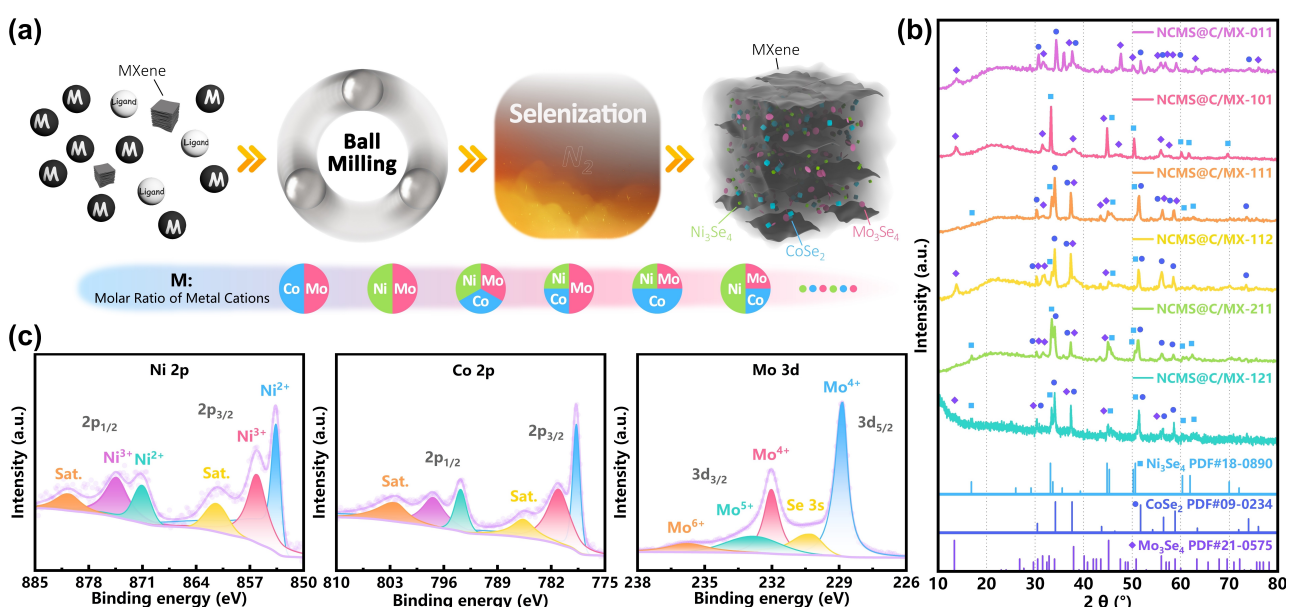


Figure 1. a) Schematic diagram of the synthesis procedure of NCMS@C/MX. b) PXRD diffraction spectra of NCMS@C/MX with different metal ratios. c) XPS spectra of NCMS@C/MX-121: Ni 2p, Co 2p and Mo 3d.

121, the XRD results of the remaining trimetal-centered MOF-derived selenides showed the same phase compositions but with different peak intensities. Two bimetallic MOF-derived composite materials, NCMS@C/MX-011 and NCMS@C/MX-101, are composed of $\text{CoSe}_2\&\text{Mo}_3\text{Se}_4$, and $\text{Ni}_3\text{Se}_4\&\text{Mo}_3\text{Se}_4$, respectively.

The influences of different metal salts feeding ratios during the preparation procedure on the XRD spectra of the final composites are shown in Figure S1. By comparing the XRD of NCMS@C/MX-011, NCMS@C/MX-111, and NCMS@C/MX-211, it can be found that the peak intensities of Ni_3Se_4 at 33.152° , 33.665° , 44.832° , 45.305° , 50.225° , and 50.673° also gradually increase as the proportion of Ni element increases (Figure S1a). Figure S1b shows a similar situation for CoSe_2 in NCMS@C/MX-101, NCMS@C/MX-111, and NCMS@C/MX-121 composites. The intensities of Mo_3Se_4 peaks at 31.543° and 56.027° between NCMS@C/MX-111 and NCMS@C/MX-112 composites are also positively correlated with the addition ratio of Mo salts (Figure S1c). This result suggests that the compositions of multi-metal selenides@C/MXene can be tuned via their multivariate MOF/MXene precursors prepared by the mechanochemical ball-milling method. What is worth mentioning is that, the characteristic peaks of MXene at 5° – 10° could not be found for all the composites (Figure S1d). This phenomenon indicates that the exfoliated MXene flakes have been evenly dispersed in the as-prepared composites.^[44]

X-ray photoelectron spectroscopy (XPS) was used to perform a full-range scan of the elemental composition of NCMS@C/MX-121 (Figure S2a). The existence of elements such as C, O, Ni, Co, Mo, Se, Ti, N, and P are proven in NCMS@C/MX-121 composite. Furthermore, XPS fine spectrum characterization was performed on NCMS@C/MX-121 to obtain the oxidation state details of above elements. Figure 1(c) shows the fine XPS spectrum of Ni 2p, and the coexistence of Ni^{2+} and Ni^{3+} can be seen.^[45,46] In the fine XPS spectrum of Co 2p, two sets of peaks related to Co 2p_{3/2} (778.73 eV, 781.04 eV) and Co 2p_{1/2} (793.80 eV, 797.38 eV) can be found along with two satellite peaks. This indicates the presence of Co^{2+} and Co^{3+} in NCMS@C/MX-121.^[47] For the Mo element, multiple oxidate states (Mo^{4+} , Mo^{5+} , and Mo^{6+}) are found, implying the successful synthesis of Mo_3Se_4 .^[45,48,49] According to the high-resolution XPS spectrum of Se 3d (Figure S2b), the spectrum contains signals from Se^{2-} , $\text{Se}-\text{Se}$, and $\text{Se}-\text{O}$.^[45,50] Finally, graphitic N and pyridinic-N are found in N 1s spectrum (Figure S2c).^[49] The P 2p spectrum displays the simultaneous presence of P–O bonds and P=O bonds (Figure S2d).^[51,52] From the high-resolution Ti 2p spectrum, two peaks at 465.45 and 459.68 eV can be found and correspond to Ti 2p_{1/2} and Ti 2p_{3/2}, respectively (Figure S2e).^[31] These results above further proved the successful synthesis of multi-metal selenides@C/MXene composites as well as the successful doping of multi-heteroatoms in the carbon matrix.

Scanning electron microscopy (SEM) was used to study the morphologies of NCMS@C/MX composites (Figure 2a and b & Figure S3). Figure 2(a and b) shows the SEM images for NCMS@C/MX-121. The Ni_3Se_4 and CoSe_2 nanoparticles with a

size range from dozens to hundreds of nanometers and Mo_3Se_4 nanosheets are evenly distributed in the multi-heteroatom-doped carbon matrix (Figure 2a and b). The ball-milling exfoliated MXene exists as few-layer flakes inwoven in the carbon matrix, which cannot be easily spotted. These ball-milling exfoliated MXene flakes can provide a robust framework preventing not only the aggregation of MOF during the milling process but also the fusion of MOF-derived composite particles during the annealing process. Further, these MXene sheets pave the way for rapid electron transport, enhancing the overall electrochemical performance. Compared to NCMS@C/MX-121, the remaining composites (NCMS@C/MX-211, NCMS@C/MX-112, NCMS@C/MX-111, NCMS@C/MX-101, and NCMS@C/MX-011) have similar morphology and composition structure (Figure S3). Therefore, the morphology-related influence on later investigated sodium-ion storage performance can be ruled out. This result further illustrates that the obtained electrochemical performance of these prepared composites strongly depends on their compositions.

To gain further detailed morphology and composition information on NCMS@C/MX-121 (Figures 2c and d, S4). Transmission electron microscopy (TEM) was applied. As shown in Figure 2(c and d), dark Ni_3Se_4 and CoSe_2 particles, and Mo_3Se_4 sheet-like structures are distributed on the light grey-colored carbon matrix. In high-resolution TEM images, interlayer spacing of 0.267 nm corresponding to Ni_3Se_4 and the spacing of 0.240 nm corresponding to CoSe_2 (211) can be easily spotted. Clear two-dimensional lattice fringes (020) and (210) of the Mo_3Se_4 phase can also be found in Figure 2(d). Reviewing previous XRD results, it can be concluded that ball-milling prepared Ni, Co, and Mo trimetal-centered MOF/MXene composites were successfully derived into corresponding multiple selenides composites rich in heterojunction structures. This is further confirmed by the selected area electron diffraction (SAED) results (Figure S4). Those heterojunction structures are reported to be beneficial for charge transfer and sodium-ion adsorption.^[53,54]

The TEM elemental mapping results are shown in Figure 2(e) and in good consistent with the SEM and TEM results. Ni, Co, and Se elements are distributed mainly on Ni_3Se_4 and CoSe_2 particles. Mo and Ti are widely distributed in the composites due to the sheet-like structure of Mo_3Se_4 and exfoliated MXene flakes. Uniform distribution of elements C, N, O, and P are observed for NCMS@C/MX-121, indicating successful multiple heteroatoms doping in the carbon matrix.

Combining the analysis results above, it can be concluded that NCMS@C/MX-121 composites are rich in heterojunction structures built between Ni_3Se_4 , CoSe_2 , and Mo_3Se_4 phases. These particles and nanosheets are mounted in a multi-heteroatoms doped carbon matrix. Exfoliated MXene flakes are inwoven in the carbon matrix. The MXene sheets and carbon matrix together would provide a highway for electron transfer and alleviate volume expansion during the charging and discharging process. Besides, the phase boundaries in heterojunction structures can form an internal self-built

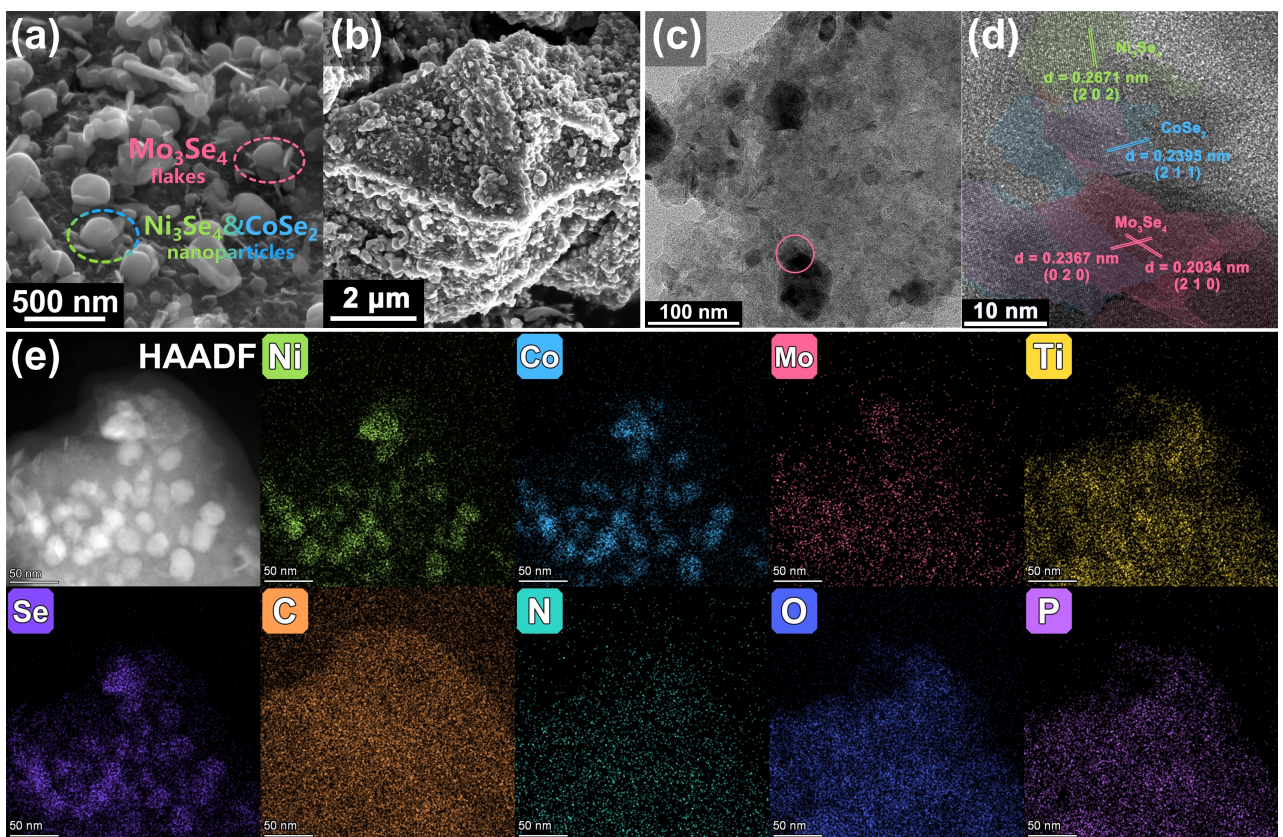


Figure 2. NCMS@C/MX-121: a, b) SEM, c) TEM image, d) HR-TEM photo, and e) Mapping.

electric field and enhance the reaction kinetics effectively during the charging and discharging process, further promoting the electron transfer process. As a result, high sodium-ion storage performance for NCMS@C/MX-121 is expected.^[55]

Sodium-ion storage properties

To evaluate their electrochemical properties, the as-prepared NCMS@C/MX composites are assembled into sodium-ion half-cells. Figure 3(a) shows the first four CV curves of a sodium-ion half-cell with NCMS@C/MX-121 electrode. During the first discharge cycle, two sharp peaks at 1.12 and 1.01, and a broad peak at 0.62 V represent the insertion of sodium ions into NCMS@C/MX-121, as well as the formation of solid electrolyte interface (SEI) film.^[56–58] The sharp peaks at 1.01 and 1.12 V are due to the activation process.^[57,58] The reduction peak at 0.62 V is related to the formation of Ni, Co, Na_2Se , and SEI.^[56] During the charging scan, there are two adjacent peaks at 1.77 and 1.83 V related to the formation of Na_xCoSe_2 and CoSe_2 .^[57] Based on the subsequent cycles, the sodium-ion storage mechanism can be divided into three steps. The most obvious reduction peak appeared at 1.45 V corresponds to the insertion step: $\text{CoSe}_2 + x\text{Na}^+ + xe^- \rightarrow \text{Na}_x\text{CoSe}_2$, and the reduction peak at 1.12 V relates to the conversion step: $\text{Na}_x\text{CoSe}_2 + (2-x)\text{Na}^+ + (2-x)e^- \rightarrow \text{CoSe} + \text{Na}_2\text{Se}$.^[57] While the peak at 0.74 V corresponds to the

formation of $\text{Co}/\text{Na}_2\text{Se}$.^[57,58] During the charging process, only one obvious oxidation peak appears at 1.83 V, indicating the removal of Na^+ from the electrode.^[59,60] The electrochemical behavior of NCMS@C/MX-121 electrode mimics CoSe_2 kind materials a lot due to the higher content of CoSe_2 . The CV curves of second to fourth cycles basically overlapped, proving good electrochemical reversibility of NCMS@C/MX-121 electrode.

Figure 3(b) shows charge-discharge curves of the first five cycles for NCMS@C/MX-121 electrode. The initial discharge and charge specific capacities are 615.22 and 437.52 mAh g^{-1} , respectively, indicating an initial columbic efficiency of 71.1%. Large initial capacity loss is mainly due to irreversible structural damage caused by sodium insertion during the first cycle and SEI film formation. In the following cycles, the almost overlapped specific capacity-voltage curves indicate good structural stability. Moreover, compared to the GCD curves of NCMS@C/MX-121, the redox peaks in the CV profiles matched well with the charge-discharge platforms.

To evaluate the influence of composition on the sodium-ion storage properties of NCMS@C/MX electrodes. The specific capacities and reversibility of these electrodes were tested with an operation window of 0.01–3.0 V. Figure 3(c) shows the rate performance comparison between NCMS@C/MX electrodes. Overall, all electrodes show relatively good rate capability due to their similar composited structures. Close analysis of the results shows that the trimetal

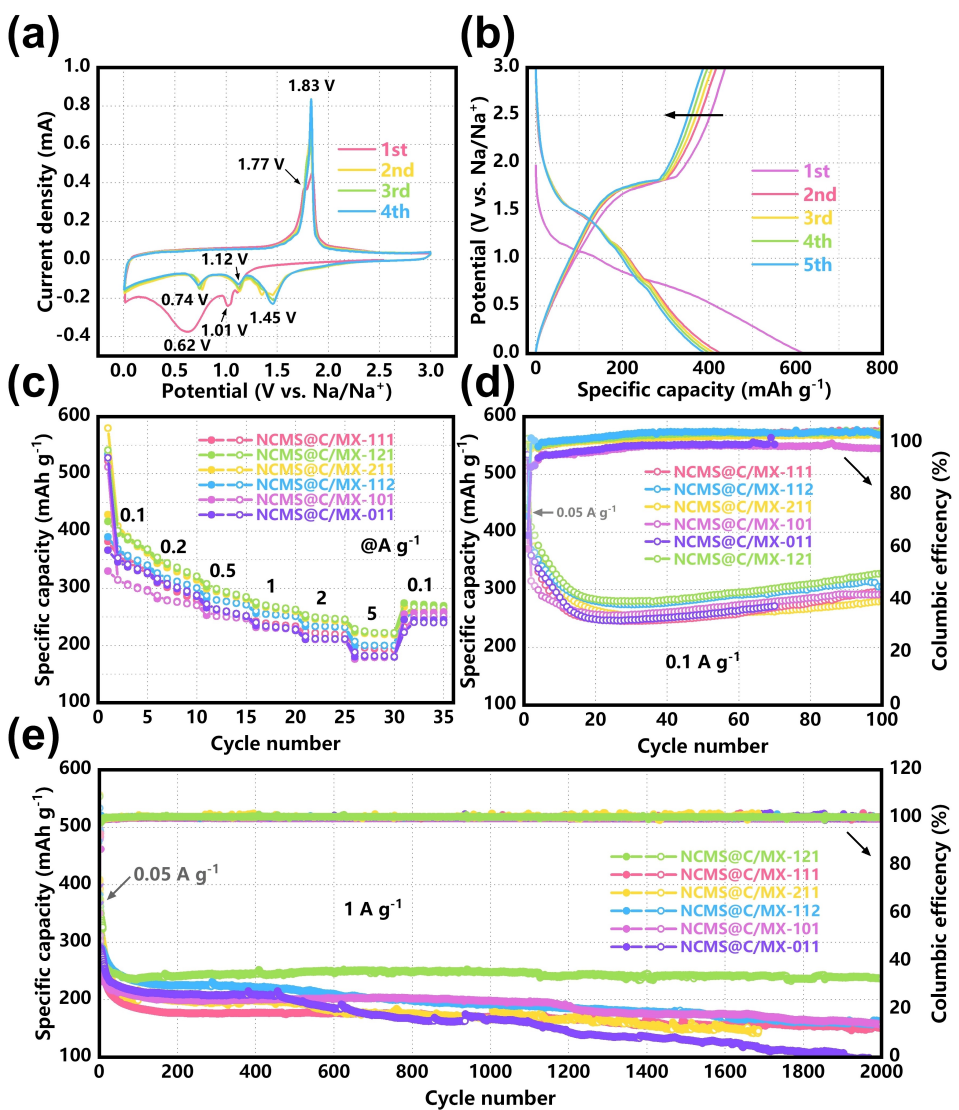


Figure 3. Electrochemical performance of NCMS@C/MX-121, NCMS@C/MX-211, NCMS@C/MX-112, NCMS@C/MX-111, NCMS@C/MX-101 and NCMS@C/MX-011 for SIBs: a) Initial four CV curves of NCMS@C/MX-121 electrode, b) GCD voltage curves of NCMS@C/MX-121 electrode, c) rate capability comparison and cycling stability of NCMS@C/MX electrodes at d) 0.1, and e) 1 Ag⁻¹.

NCMS@C/MX electrodes present overall higher capacities and better rate capabilities than those of bimetallic NCMS@C/MX electrodes. At current densities of 0.1, 0.2, 0.5, 1, 2, and 5 Ag⁻¹, the trimetal NCMS@C/MX-121 electrode shows the highest discharge specific capacities of 400.62, 353.94, 307.85, 275.63, 253.49, and 229.24 mAh g⁻¹, respectively. While, the bimetallic NCMS@C/MX-101 electrode only shows 305.44, 275.89, 250.07, 230.48, 210.61, and 179.19 mAh g⁻¹, respectively. This is probably due to the more abundant phase boundaries in heterojunction structures of trimetal NCMS@C/MX composites. Further comparing among trimetal NCMS@C/MX electrodes shows that those electrodes with bigger Ni or Co contents (e.g., NCMS@C/MX-211 and NCMS@C/MX-121) possess higher capacities at all current densities. This result may mainly correlate to the much lighter atomic weight of Ni and Co than Mo.

Long-term cycling stability of all composite materials at 0.1 and 1 Ag⁻¹ current densities were evaluated (Figure 3d and e). Before the long-term cycling tests at 0.1 Ag⁻¹ and 1 Ag⁻¹, the half cells were activated at 0.05 Ag⁻¹ for three loops. Apparent capacity loss can be observed at both current densities for the initial dozens of cycles. This might be caused by the structural collapse of nanostructured selenides, especially those exposed on the surface of the composites. Leaving the initial capacity loss aside, better capacity retentions are found for NCMS@C/MX electrodes with bigger Co or Mo contents (e.g., NCMS@C/MX-121 and NCMS@C/MX-112). The composite NCMS@C/MX-211 with bigger Ni content presents high initial capacity but much faster capacity loss. This phenomenon could be related to the intrinsic properties of different metal selenides. For example, nickel selenides normally show high sodium-ion storage reactivity, while cobalt selenides and molybdenum selenides

often exhibit excellent structural stabilities.^[61,62] Taken together, the NCMS@C/MX-121 electrode with Ni:Co:Mo ratio of 1:2:1 possesses both higher initial capacity and better capacity retention than the others. Furthermore, a capacity of 328.96 mAh g⁻¹ was obtained after 100 cycles at 0.1 A g⁻¹ (Figure 3d). At a higher current density of 1 A g⁻¹, the NCMS@C/MX-121 also maintained a high capacity of 236.69 mAh g⁻¹ after 2000 cycles, while the capacities of other electrodes decreased dramatically (Figure 3e). In conclusion, the electrochemical performance of NCMS@C/MX electrodes derived from multivariate MOF/MXene composites can be tuned precisely by controlling their metal salt feeding ratios.

To further reveal the electrochemical reaction kinetic characteristics of the NCMS@C/MX-121 electrode, we studied the CV curves at different scan rates. As shown in Figure 4(a). As the scan rate rises, the shape of the CV curve remains basically unchanged, and the redox peaks widen gradually. The relationship between peak current (*i*) and scan rate (*v*) can be described as $i = av^b$.^[63] *b* is a constant value with a normal range of 0.5–1.0, where 0.5 represents diffusion control behavior and 1.0 represents the surface capacitive control behavior. For NCMS@C/MX-121 electrode, the *b* values of the peaks are 1.38, 0.56, 0.90, 0.81, 1.39, 0.18, and 1.30, respectively (Figure 4b), indicating the coexistence of redox reaction and pseudocapacitance phenomena. The percentage of pseudocapacitance contribution can be calcu-

lated using the following equation:^[64] $I(v) = k_1 v^{1/2} + k_2 v$. When the scan rate rises from 0.2 to 1.0 mV s⁻¹, the contribution of pseudocapacitance rises from 75.2% to 93.5% of the total capacity (Figure 4c and d), indicating an overall high pseudocapacitance contribution, especially at high current densities. This high pseudocapacitance contribution normally favors the rate capability and cycling performance of electrodes.

Last but not least, we found that NCMS@C/MX-121 electrode performs comparably with analogues prepared by other methods. For example, compared with the previously reported hollow skeletons CoSe₂@C \cap NC, it shows a capacity of 324 mAh g⁻¹ after 200 cycles at 0.1 A g⁻¹. The herein presented NCMS@C/MX-121 composite exhibits a comparable specific capacity (329 mAh g⁻¹) after 100 cycles at the same current density.^[65] When compared with Ni₃Se₄@CoSe₂@C/CNTs, NCMS@C/MX-121 electrode presents a capacity of 236 mAh g⁻¹ after 2000 cycles at a current density of 1 A g⁻¹. However, for Ni₃Se₄@CoSe₂@C/CNTs, the capacity drops to a similar level after only 600 cycles.^[56] Therefore, it is believed that the NCMS@C/MX composites prepared via the herein-described strategy have a great potential for applications in the sodium-ion storage field (Table S1).

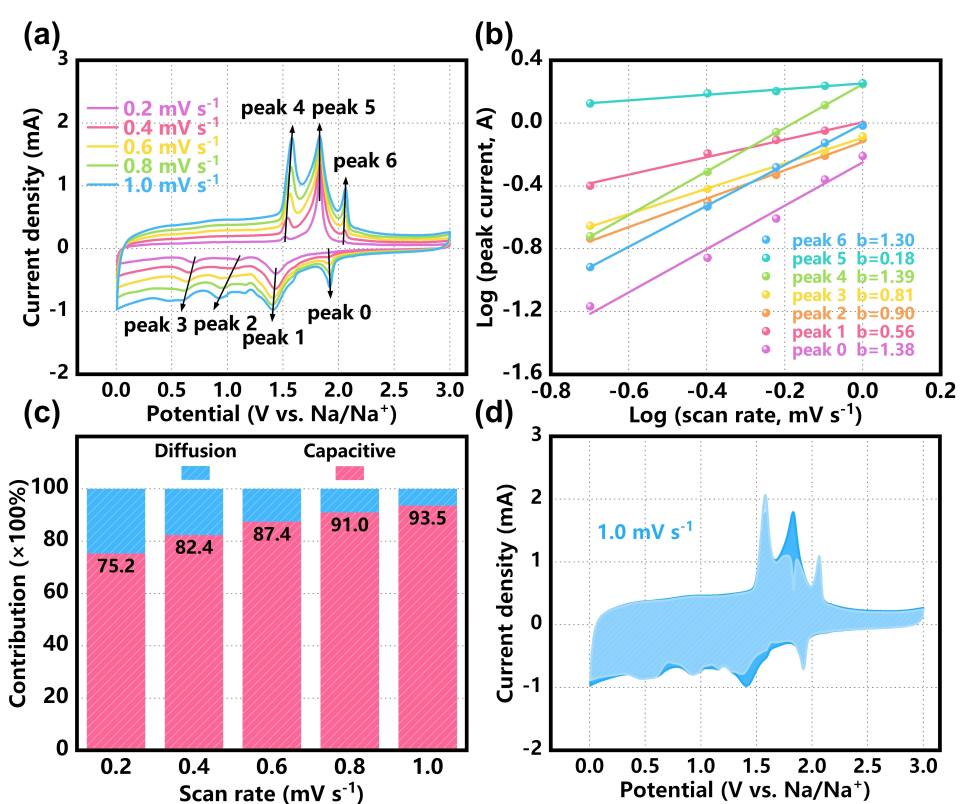


Figure 4. Electrochemical reaction dynamics analysis of the NCMS@C/MX-121 for sodium storage: a) CV curves at different scan rates, b) functional relationship of $\log(i)$ versus $\log(v)$ at each redox peak, c) normalized percentage of pseudocapacitance at different scan rates and d) the pseudocapacitance contribution to the total current at a scan rate of 1.0 mV s⁻¹.

Conclusions

In summary, this work proposes an atom economic mechanochemical ball milling method to realize the efficient component regulation of target multivariate MOFs/MXene composites. MOF/MXene-derived NCMS@C/MX composites are proved to be multiple nanostructured metal selenides embedded in multi-heteroatom doped carbon matrix as expected. For these composites, abundant heterojunction structures are formed. This heterojunction structure can build internal self-built electric field and enhance the reaction kinetics effectively for sodium-ion storage. Besides, the multi-heteroatom doped carbon matrix together with the exfoliated MXene flakes inwoven therein could play a highway in electron transfer and alleviate the volume expansion during the charge/discharge processes. Above mentioned characteristics endow the NCMS@C/MX composites with relatively good rate capability and structural reversibility. More importantly, by changing the feeding ratio of the metal salts during the synthesis of the multivariate MOFs/MXene composites, the electrochemical performance of NCMS@C/MX composites can be optimized due to the intrinsic characteristics of the containing metal selenides.

Overall, experimental results demonstrate the universality of this novel solvent-free synthesis route for controllable preparation of high-performance multivariate MOF/MXene-derived electrode materials. It provides a feasible and environmentally friendly method to adjust metal ratios for optimal energy storage performance.

We hope this research inspires optimization strategies for high-performance electrode materials and leads to the development of energy storage materials with more rational structures and better performance.

Experimental Section

Materials

Nickel(II) acetate tetrahydrate (99.0%), Cobalt(II) acetate tetrahydrate (99.9%), and Selenium powder (95%) were all purchased from Aladdin. Molybdenum(V) chloride is purchased from Macklin. MXene is purchased from 11 Technology Co., Ltd. All chemicals were used directly upon receipt.

Materials characterization

A Rigaku D/MAX-Ultima IV diffractometer was used to collect the X-ray diffraction spectrum, using Cu-K α radiation and a wavelength of 0.15406 nm. The sample's morphology was examined using a Hitachi SU8010 field emission scanning electron microscope. The transmission electron microscope (Tecnai G2 F30, FEI, USA), equipped with HAADF-STEM and EDX (AMETEK Inc., PA, USA), was used to obtain microstructure and element mapping distribution. The composition elements were analyzed using X-ray photoelectron spectroscopy with a Thermo Scientific ESCA-LAB 250Xi spectrometer.

Synthesis of NCMS@C/MX

Nickel(II) acetate tetrahydrate, cobalt acetate tetrahydrate, molybdenum pentachloride, 200 mg hexa(4-carboxyphenoxy)cyclotriphosphonitrile (ligand), and MXene with 10% of the total mass of the above materials were sealed in a zirconium dioxide ball mill jar under an inert gas atmosphere. The M-MOF/MX composites were obtained by ball milling at 1800 rpm for 2 h. The resulting complex was selenized with 3 times its mass of selenium powder and warmed up to 650 °C at a heating rate of 1 °C min $^{-1}$ under a nitrogen atmosphere and held for 3 h. Among them, the molar ratio of the addition of metal salt: hexa(4-carboxyphenoxy)cyclotriphosphonitrile was always kept constant at 3:1 during the synthesis of each composite. For example, the additions of nickel(II) acetate tetrahydrate, cobalt acetate tetrahydrate, molybdenum pentachloride, and MXene for NCMS@C/MX-121 were 39.0 mg, 78.0 mg, 42.8 mg, and 36.0 mg, respectively. 121 is the molar ratio of transition metals in the three metal salts: N for Ni, C for Co, M for Mo, and S for Se. The remaining NCMS@C/MX-111, NCMS@C/MX-211, NCMS@C/MX-112, NCMS@C/MX-101, and NCMS@C/MX-011 and so on. It should be noted that only two metal salts were added to both NCMS@C/MX-101 and NCMS@C/MX-011, with 0 indicating that no such metal salt was added. The molar ratios between the metal cations and between the ligands follow the aforementioned laws.

Electrochemical measurements

Weigh out the composite, PVDF (polyvinylidene fluoride), and conductive carbon black in an 8:1:1 mass ratio. Mix and grind finely until the mixture is uniform and the particles are small. Gradually add an appropriate amount of N-methylpyrrolidone (NMP) dropwise, and continue grinding to obtain a uniformly dispersed slurry. Transfer the slurry to the rough surface of the collector (copper foil). Spread it evenly with a scraper and dry it under a vacuum. After drying, cut the coated pieces into circular electrode pieces with a diameter of 12 mm. Weigh them one by one to calculate the amount of active material. The electrodes with active material loading mass around 1.0 mg cm $^{-2}$ were selected. Place the electrode pieces in a glove box and assemble them into button cells. The electrolyte used for the sodium-ion half-cell is NaPF₆ electrolyte (NP-005, 1 M NaPF₆ in DIGLYME = 100 Vol%), with a total addition of 150 μ L.

The electrochemical performance was tested using the NEWARE CT-4008T-5 V20 mA-164 button cell tester. The sodium-ion half-cell had a voltage range of 0.01–3.0 V. The battery underwent rate performance assessment, with current densities of 0.1, 0.2, 0.5, 1, 2, and 5 Ag $^{-1}$ in sequence. It was then returned to 0.1 Ag $^{-1}$ and cycled 5 times at each condition. For the cycle life and stability test, 0.1 Ag $^{-1}$ and 1 Ag $^{-1}$ were selected, with small current cycling for 100 cycles and large current cycling for 3000 cycles. The data for the GCD were taken from the rate performance test at the corresponding 0.1 Ag $^{-1}$.

Cyclic voltammetry testing was performed using an electrochemical workstation (CHI760E, Shanghai, China). The voltage range for the sodium-ion half-cell was set to the same as above, with a scan rate of 0.1 mVs $^{-1}$ and continuous cycling for 4 cycles. Cyclic voltammetry was tested at different scan rates of 0.2, 0.4, 0.6, 0.8, and 1.0 mVs $^{-1}$, respectively. Each scan speed was operated for 3 cycles.

Supporting Information

The authors have cited additional references within the Supporting Information.^[56,60,65–67]

Author Contributions

Weiquan Liang: Investigation, Validation, Data curation, Formal analysis, Visualization, Writing - original draft. **Mingjie Liu:** Investigation. **Xiaoyan Shi:** Conceptualization, Data curation, Formal analysis, Funding acquisition, Methodology, Validation, Writing - review & editing. **Bin Chen:** Investigation. **Lianyi Shao:** Visualization. **Junling Xu:** Visualization. **Zhipeng Sun:** Validation, Resources, Project administration, Supervision, Funding acquisition.

Acknowledgements

We would like to thank Analysis and Test Center, Guangdong University of Technology for microstructure characterization. This work was supported by the National Natural Science Foundation of China [No. 22271066]; Guangzhou Science and Technology Planning Project [No. 202201010236].

Conflict of Interests

The authors declare that they have no known competing financial interests or personal relationships that could have appeared to influence the work reported in this paper.

Data Availability Statement

Data will be made available on request.

Keywords: controlled synthesis · electrochemical properties · mechanochemical ball-milling · multivariate MOFs · sodium-ion storage

- [1] X. Xie, K. Huang, X. Wu, N. Wu, Y. Xu, S. Zhang, C. Zhang, *Carbon* **2020**, *169*, 1–8.
- [2] Y. Wang, Z. Wen, C. C. Wang, C. C. Yang, Q. Jiang, *Small* **2021**, *17*, 2102349.
- [3] H. Li, T. Wang, X. Wang, G. Li, J. Shen, J. Chai, *Electrochim. Acta* **2021**, *373*, 137905.
- [4] A. Li, P. Xiong, Y. Zhang, W. Shuang, Z. Chang, Y. Xu, X.-H. Bu, *Chem. Eng. J.* **2021**, *405*, 126638.
- [5] X. Shi, Q. Liu, W. Liang, B. Chen, L. Shao, J. Cai, Z. Sun, Y. Zhang, H. Huang, Y. Wu, *Mater. Today Sustain.* **2022**, *18*, 100151.
- [6] W. Liang, B. Chen, W. Lin, L. Shao, X. Shi, Z. Sun, *Mater. Lett.* **2023**, *332*, 133542.
- [7] X. Wang, C. Chen, F. Ichihara, M. Oshikiri, J. Liang, L. Li, Y. Li, H. Song, S. Wang, T. Zhang, Y. Huang, R. Cao, J. Ye, *Appl. Catal. B* **2019**, *253*, 323–330.
- [8] L. Han, X. Liu, X. Zhang, M. Li, D. Li, P. Qin, S. Tian, M. Lu, Z. Cai, J. Hazard. Mater. **2022**, *424*, 127559.

- [9] H. Liu, H. Guo, N. Wu, W. Yao, R. Xue, M. Wang, W. Yang, *J. Alloys Compd.* **2021**, *856*, 156535.
- [10] I. Abánades Lázaro, C. J. R. Wells, R. S. Forgan, *Angew. Chem. Int. Ed.* **2020**, *59*, 5211–5217.
- [11] Y. Jin, H. Lu, B. Yan, *Dyes Pigm.* **2021**, *194*, 109588.
- [12] A. Ma, H. Cong, H. Deng, *Green Energy & Environ.* **2022**, *7*, 575–577.
- [13] R. Ma, H. Jiang, C. Wang, C. Zhao, H. Deng, *Chem. Commun.* **2020**, *56*, 2715–2718.
- [14] Z. Zheng, N. Hanikel, H. Lyu, O. M. Yaghi, *J. Am. Chem. Soc.* **2022**, *144*, 22669–22675.
- [15] L. Han, X. Zhang, D. Li, M. Li, P. Qin, S. Tian, Y. Wang, M. Lu, Z. Cai, *Talanta* **2021**, *235*, 122818.
- [16] X. Li, Y. Yao, B. Wang, *Chem. Eng. J.* **2022**, *446*, 137446.
- [17] S. Głowniak, B. Szczęśniak, J. Choma, M. Jaroniec, *Mater. Today* **2021**, *46*, 109–124.
- [18] S. Martínez, L. Veth, B. Lainer, P. Dydio, *ACS Catal.* **2021**, *11*, 3891–3915.
- [19] K. Užarević, T. C. Wang, S. Y. Moon, A. M. Fidelli, J. T. Hupp, O. K. Farha, T. Frisčić, *Chem. Commun.* **2016**, *52*, 2133–2136.
- [20] P. He, Z. Hu, Z. Dai, H. Bai, Z. Fan, R. Niu, J. Gong, Q. Zhao, T. Tang, *ChemSusChem* **2023**, *16*, e202201935.
- [21] Z. W. Zhu, Q. R. Zheng, *Int. J. Hydrogen Energy* **2023**, *48*, 5166–5174.
- [22] M. Y. B. Zulkifli, Y. Yao, R. Chen, M. Chai, K. Su, X. Li, Y. Zhou, R. Lin, Z. Zhu, K. Liang, V. Chen, J. Hou, *Chem. Commun.* **2022**, *58*, 12297–12300.
- [23] W. Zhang, Z. Shahnavaz, X. Yan, X. Huang, S. Wu, H. Chen, J. Pan, T. Li, J. Wang, *Inorg. Chem.* **2022**, *61*, 15287–15301.
- [24] F. M. Jais, S. Ibrahim, C. Y. Chee, Z. Ismail, *J. Environ. Chem. Eng.* **2021**, *9*, 106367.
- [25] A. A. Bhoite, K. V. Patil, R. S. Redekar, P. S. Patil, V. A. Sawant, N. L. Tarwal, *J. Solid State Chem.* **2023**, *326*, 124192.
- [26] X. Shi, W. Liang, G. Liu, B. Chen, L. Shao, Y. Wu, Z. Sun, F. García, *Chem. Eng. J.* **2023**, *462*, 1–11.
- [27] D. Sun, F. Sun, X. Deng, Z. Li, *Inorg. Chem.* **2015**, *54*, 8639–8643.
- [28] A. VahidMohammadi, J. Rosen, Y. Gogotsi, *Science* **2021**, *372*, eabf1581.
- [29] M. Naguib, M. W. Barsoum, Y. Gogotsi, *Adv. Mater.* **2021**, *33*, 2103393.
- [30] X. Yu, Y. Yang, L. Si, J. Cai, X. Lu, Z. Sun, *J. Colloid Interface Sci.* **2022**, *627*, 992–1002.
- [31] F. Qi, L. Shao, X. Lu, G. Liu, X. Shi, Z. Sun, *Appl. Surf. Sci.* **2022**, *605*, 154653.
- [32] J. Guan, L. Shao, L. Yu, S. Wang, X. Shi, J. Cai, Z. Sun, *Chem. Eng. J.* **2022**, *443*, 136502.
- [33] X. Zhuang, S. Zhang, Y. Tang, F. Yu, Z. Li, H. Pang, *Coord. Chem. Rev.* **2023**, *490*, 215208.
- [34] Y. Wu, P. Nie, L. Wu, H. Dou, X. Zhang, *Chem. Eng. J.* **2018**, *334*, 932–938.
- [35] S. Sun, C. Liao, A. M. Hafez, H. Zhu, S. Wu, *Chem. Eng. J.* **2018**, *338*, 27–45.
- [36] J. Tang, X. Huang, T. Lin, T. Qiu, H. Huang, X. Zhu, Q. Gu, B. Luo, L. Wang, *Energy Storage Mater.* **2020**, *26*, 550–559.
- [37] Y. Lei, Z. Yan, W. Lai, S. Chou, Y. Wang, H. Liu, S. Dou, *Electrochem. Energy Rev.* **2020**, *3*, 766–792.
- [38] R. Zang, P. Li, G. Wang, *Chem. Res. Chin. Univ.* **2020**, *36*, 431–438.
- [39] Y. Gu, X. Li, G. Ye, Z. Gao, W. Xu, Y. Sun, *New J. Chem.* **2021**, *45*, 9591–9597.
- [40] M. Taheri, I. D. Bernardo, A. Lowe, D. R. Nisbet, T. Tsuzuki, *Cryst. Growth Des.* **2020**, *20*, 2761–2773.
- [41] R. Wang, X. Y. Dong, J. Du, J. Y. Zhao, S. Q. Zang, *Adv. Mater.* **2018**, *30*, 1703711.
- [42] P. Sun, J. Zhang, J. Huang, L. Wang, P. Wang, C. Cai, M. Lu, Z. Yao, Y. Yang, *Mater. Res. Bull.* **2021**, *137*, 111196.
- [43] X. Shi, J. Yu, Q. Liu, L. Shao, J. Cai, Z. Sun, *Sustain Mater Techno* **2021**, *28*, e00275.
- [44] E. Xu, P. Li, J. Quan, H. Zhu, L. Wang, Y. Chang, Z. Sun, L. Chen, D. Yu, Y. Jiang, *Nano-Micro Lett.* **2021**, *13*, 40.
- [45] M. Palanisami, K. Kaur, B. K. Sahu, S. Kataria, M. Chandel, A. Sharma, S. Elumalai, R. Ramaraj, V. Shanmugam, *Microchem. J.* **2022**, *183*, 108078.
- [46] J. Du, Z. Zou, C. Liu, C. Xu, *Nanoscale* **2018**, *10*, 5163–5170.
- [47] H. Yuan, H. Peng, B. Li, J. Xie, L. Kong, M. Zhao, X. Chen, J. Huang, Q. Zhang, *Adv. Energy Mater.* **2019**, *9*, 1802768.
- [48] H. Guo, H. Guo, Y. Xie, Y. Chen, C. Lu, Z. Yang, Y. Zhu, Y. Ouyang, Y. Zhang, X. Wang, *Redox. Biol.* **2022**, *56*, 102441.
- [49] J. Chen, Y. Luo, W. Zhang, Y. Qiao, X. Cao, X. Xie, H. Zhou, A. Pan, S. Liang, *Nano-Micro Lett.* **2020**, *12*, 171.
- [50] B. Zhan, S. Butt, Y. Liu, J. Lan, C. Nan, Y. Lin, *J. Electroceram.* **2015**, *34*, 175–179.
- [51] C. X. Yan, R. G. Cavell, *J. Electron Spectrosc. Relat. Phenom.* **1987**, *42*, 49–60.

- [52] R. Franke, T. Chassé, P. Streubel, A. Meisel, *J. Electron Spectrosc. Relat. Phenom.* **1991**, *56*, 381–388.
- [53] G. Li, M. Song, X. Zhang, Y. Sun, J. Guo, *Dalton Trans.* **2023**, *52*, 4973–4979.
- [54] E. Xu, Y. Zhang, H. Wang, Z. Zhu, J. Quan, Y. Chang, P. Li, D. Yu, Y. Jiang, *Chem. Eng. J.* **2020**, *385*, 123839–123849.
- [55] L. Cao, X. Liang, X. Ou, X. Yang, Y. Li, C. Yang, Z. Lin, M. Liu, *Adv. Funct. Mater.* **2020**, *30*, 1910732.
- [56] H. Zhu, Z. Li, F. Xu, Z. Qin, R. Sun, C. Wang, S. Lu, Y. Zhang, H. Fan, *J. Colloid Interface Sci.* **2022**, *611*, 718–725.
- [57] X. Cheng, D. Li, F. Liu, R. Xu, Y. Yu, *Small Methods* **2019**, *3*, 1800170.
- [58] X. Yun, T. Lu, R. Zhou, Z. Lu, J. Li, Y. Zhu, *Chem. Eng. J.* **2021**, *426*, 131328.
- [59] X. Ma, L. Zou, W. Zhao, *Chem. Commun.* **2018**, *54*, 10507–10510.
- [60] Y. Gan, H. He, M. Mu, J. Yuan, H. Liao, X. Li, Y. Yu, X. Zhang, J. Liu, *J. Alloys Compd.* **2022**, *923*, 166462.
- [61] Y. K. Sun, Z. Chen, H. J. Noh, D. J. Lee, H. G. Jung, Y. Ren, S. Wang, C. S. Yoon, S. T. Myung, K. Amine, *Nat. Mater.* **2012**, *11*, 942–7.
- [62] M. Li, J. Lu, *Science* **2020**, *367*, 979–980.
- [63] M. Yan, P. He, Y. Chen, S. Wang, Q. Wei, K. Zhao, X. Xu, Q. An, Y. Shuang, Y. Shao, K. T. Mueller, L. Mai, J. Liu, J. Yang, *Adv. Mater.* **2018**, *30*, 1703725.
- [64] N. Zhang, M. Jia, Y. Dong, Y. Wang, J. Xu, Y. Liu, L. Jiao, F. Cheng, *Adv. Funct. Mater.* **2019**, *29*, 1807331.
- [65] B. Li, Y. Liu, X. Jin, S. Jiao, G. Wang, B. Peng, S. Zeng, L. Shi, J. Li, G. Zhang, *Small* **2019**, *15*, 1902881.
- [66] H. Yin, H.-Q. Qu, Z. Liu, R.-Z. Jiang, C. Li, M.-Q. Zhu, *Nano Energy* **2019**, *58*, 715–723.
- [67] Y. Zhang, S. Wei, Z. Zhao, X. Pei, W. Zhao, J. Wang, X. Du, D. Li, *Small* **2022**, *18*, 2107258.

Manuscript received: October 9, 2023

Revised manuscript received: November 8, 2023

Accepted manuscript online: November 10, 2023

Version of record online: December 19, 2023